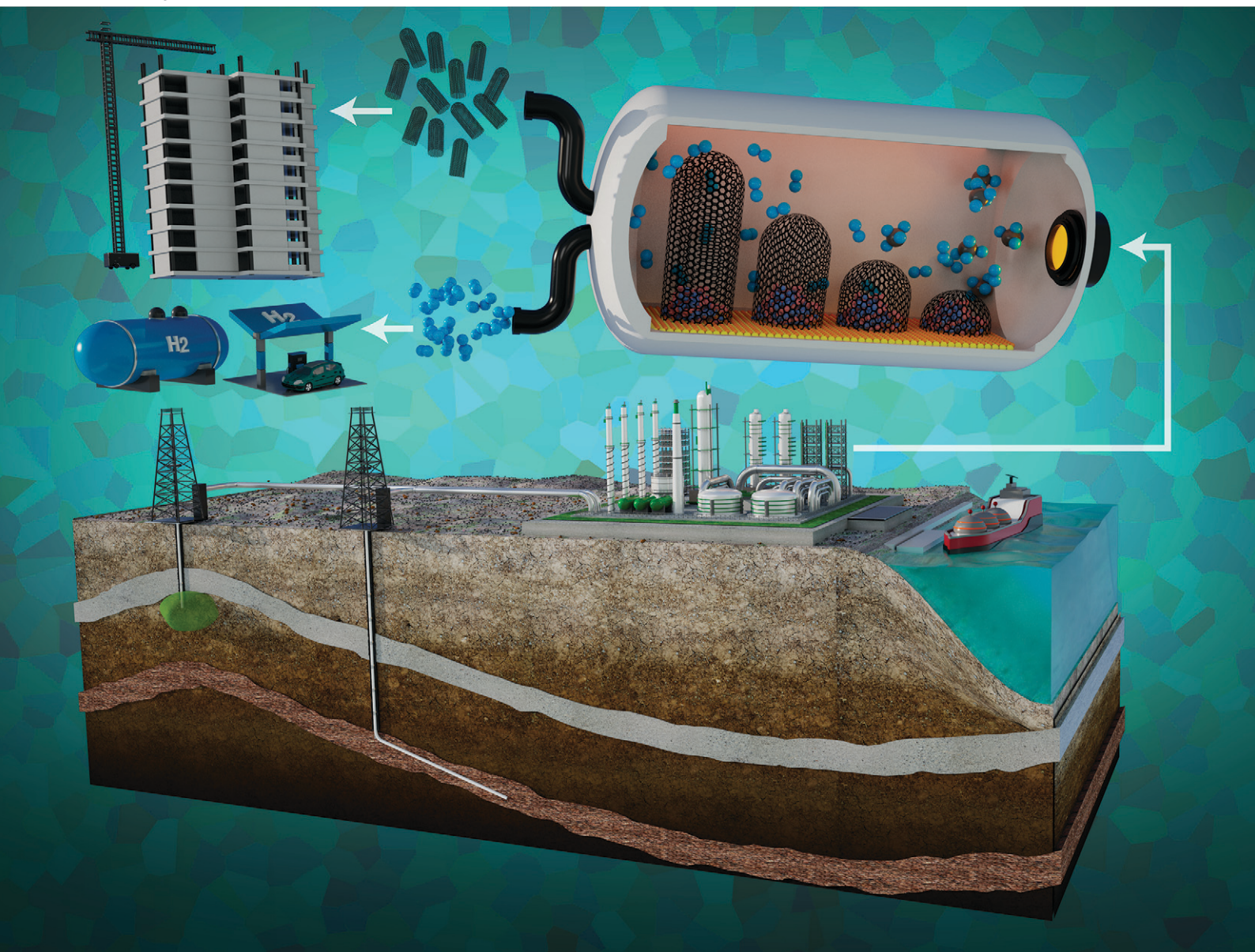


# Catalysis Science & Technology

Volume 13  
Number 11  
7 June 2023  
Pages 3195–3458

rsc.li/catalysis










ISSN 2044-4761

**PAPER**

Robert A. Dagle *et al.*  
Promotional role of NiCu alloy in catalytic performance  
and carbon properties for CO<sub>2</sub>-free H<sub>2</sub> production from  
thermocatalytic decomposition of methane

Cite this: *Catal. Sci. Technol.*, 2023,  
13, 3231

# Promotional role of NiCu alloy in catalytic performance and carbon properties for CO<sub>2</sub>-free H<sub>2</sub> production from thermocatalytic decomposition of methane†

Mengze Xu,  <sup>†a</sup> Juan A. Lopez-Ruiz,  <sup>†a</sup> Nickolas W. Riedel,  <sup>†a</sup>  
Robert S. Weber, <sup>†a</sup> Mark E. Bowden,  <sup>b</sup> Libor Kovarik,  <sup>b</sup> Changle Jiang,  <sup>c</sup>  
Jianli Hu<sup>c</sup> and Robert A. Dagle  <sup>†\*a</sup>

Thermocatalytic decomposition (TCD) of methane produces CO<sub>2</sub>-free hydrogen and valuable co-product, solid carbon. In this study, a series of NiCu/CNT catalysts, prepared with varying Ni/Cu metal ratios and synthesis methods, were evaluated for methane TCD performance at various temperatures. Catalysts before and after reaction, and properties of the carbon product, were characterized to identify activity–structure relationships. At 550 °C, a 10 wt% Ni/CNT catalyst was active; however, it deactivated within 1 h of reaction at >600 °C. The addition of Cu increased its stability. At temperatures above 650 °C, only the catalyst with Cu loadings above 10 wt% remained active and stable. Catalyst characterization revealed that changes in i) Ni/Cu ratio, ii) metal particle size, and iii) operating temperature are key factors for TCD activity, stability, and carbon coproduct morphology. The carbon co-product is mainly composed of multiwalled carbon nanotubes (MWCNTs) whose morphology changes with Ni/Cu ratio and reaction temperature.

Received 14th October 2022,  
Accepted 3rd March 2023

DOI: 10.1039/d2cy01782b

rsc.li/catalysis

## Introduction

Due to its abundance, high H/C ratio, and price, natural gas is the feedstock for about 48% of the overall worldwide H<sub>2</sub> production.<sup>1,2</sup> The most commonly practiced process is steam reforming of methane (SMR), which generates H<sub>2</sub> and CO on industrial scales. It is often integrated with the water–gas-shift reaction (WGS) to convert CO and steam into CO<sub>2</sub> and additional H<sub>2</sub>.<sup>3–5</sup>

Thermocatalytic decomposition (TCD) of methane (CH<sub>4</sub>) is an alternative process for converting CH<sub>4</sub> into hydrogen (H<sub>2</sub>) and forms solid carbon as co-product.<sup>6,7</sup> TCD requires less

energy input than the net reaction of SMR, because TCD is modestly less endothermic (37.5 kJ mol<sup>-1</sup> H<sub>2</sub> vs. 41.3 kJ mol<sup>-1</sup> H<sub>2</sub>).<sup>2</sup> Although TCD consumes twice as much CH<sub>4</sub> as SMR per unit of H<sub>2</sub> produced, it offers a path to generating H<sub>2</sub> without incurring the production of any CO<sub>2</sub>. Thus, it converts a fossil fuel (methane) into H<sub>2</sub> that could be employed without increasing emissions of greenhouse gases.

Ni-based catalysts have been extensively investigated for the TCD reaction<sup>3,8–10</sup> because they exhibit higher activity (*i.e.* H<sub>2</sub> or carbon yield) than other transition metals such as Fe and Co, and produce carbon fibers or carbon nanotubes (500–700 °C).<sup>1,3</sup> A major challenge for Ni-based catalysts is their fast deactivation especially above 600 °C.<sup>2,4,11</sup> However, the TCD reaction is thermodynamically favored at higher temperature. Therefore, to enable broader application of TCD, it is critical to identify a catalyst that is stable and active at relatively high operation temperature. In our prior publication we showed, for a series of supported Ni catalysts, how Ni particle size affects both activity and stability.<sup>12</sup> We found that methane TCD turnover increases with Ni particle size. Further, larger Ni particles (*e.g.*, >20 nm) are selective toward the formation of CNTs, while small Ni particles (*e.g.*, <10 nm) are selective toward the formation of graphitic carbon layers. The formation of graphitic carbon layers block access to Ni active sites, thus deactivating the catalyst more

<sup>a</sup> Institute for Integrated Catalysis, Pacific Northwest National Laboratory, Richland, WA 99354, USA. E-mail: Robert.Dagle@pnnl.gov

<sup>b</sup> Environmental Molecular Sciences Laboratory, Pacific Northwest National Laboratory, Richland, WA 99354, USA

<sup>c</sup> Department of Chemical & Biomedical Engineering, West Virginia University, Morgantown, WV 26506, USA

† Electronic supplementary information (ESI) available: Characterization results for the fresh and spent catalysts with different Ni/Cu ratio. Characterization results for the fresh and spent catalysts prepared with different synthesis methods. Characterization results of spent catalysts with different Ni/Cu ratios run at different temperatures. See DOI: <https://doi.org/10.1039/d2cy01782b>

‡ Equal contributors.



quickly than when CNTs are produced. Additionally, the catalyst deactivation observed with time-on-stream was found to be due to the fragmentation of Ni particles into smaller particles followed by their encapsulation with graphitic carbon layers.<sup>12</sup> Thus, while larger particle sizes were found to enhance stability, deactivation is still problematic.

Use of a secondary metal as a dopant is one approach that can improve catalytic stability.<sup>6,13,14</sup> Various bimetallic catalysts have been explored, such as NiCo, NiFe, NiPd, NiMo and NiCu.<sup>15–25</sup> Enhanced catalytic stability is generally attributed to alloy formation.<sup>9,26</sup> Addition of Pd to Ni-based catalysts, for example, NiPd/Al<sub>2</sub>O<sub>3</sub>, can improve catalytic activity and stability because Pd is also active for the TCD reaction.<sup>22</sup> Studies of NiCu systems have also been reported.<sup>27–31</sup> The effects of Cu can be qualitatively described as follows: 1) doping Cu dilutes the low index sites of Ni (1 0 0 and 1 1 0) that are active for dissociation of CH<sub>4</sub> and promotes the formation of (111) sites that are active for carbon filament formation;<sup>9,32,33</sup> 2) the presence of Cu affects the morphology of produced carbon filaments. For instance, Echegoyen *et al.*<sup>27</sup> prepared Ni/MgO catalysts with different stability by using co-precipitation, impregnation and fusion methods. In all the preparation methods, addition of Cu promoted the production of H<sub>2</sub> (yield around 80 vol% close to the thermodynamic limit for 8 h on stream). NiCu/MgO catalysts produced a more ordered graphitic carbon than did the Ni/MgO catalysts. Similarly, preferential formation of larger carbon nanofibers with a broader distribution of diameters was observed over the NiCu/SiO<sub>2</sub> catalysts when compared to Ni/SiO<sub>2</sub> catalysts.<sup>28</sup> González *et al.*<sup>34</sup> studied the effect of adding Cu to unsupported Ni nanoparticles. They inferred that Cu inhibited the sintering of Ni particles and induced the formation of CNTs with a narrow diameter distribution.

In addition to improving catalytic performance at high operation temperatures, commercialization of TCD process also requires facile separation of carbon products during catalyst regeneration. Developing bimetallic catalysts on carbonaceous support promises to enable a cyclic reaction-regeneration process: carbon materials harvested after reaction can be used as the support for successive catalysts.<sup>35</sup> In our previous work with NiPd catalysts supported on CNTs, we identified alloys with optimized metal ratios that yielded excellent catalytic performance at reaction of 600 °C and that showed the feasibility of catalyst regeneration.<sup>35</sup> Here we explore the use of cheaper Cu to develop NiCu catalysts on a carbonaceous support.

Studies of NiCu catalysts for methane TCD have reported how changes in the NiCu particles during reaction as well as the operating temperature play a role in catalyst deactivation.<sup>30,31,36–40</sup> However, carefully controlled studies evaluating the effect of systematic changes in catalyst properties on catalyst performance, and especially the properties of the carbon co-product, are lacking. It remains a challenge to rationally design NiCu catalysts for TCD because of the many variables to consider: support materials, catalyst composition,

synthesis method, and reaction conditions.<sup>23,24,27,28,31,41–47</sup> In the study of a NiCu/SiO<sub>2</sub> catalyst at elevated temperatures (600–780 °C) by Li *et al.*,<sup>39</sup> with an increase of temperature, catalyst activity increased but eventually dropped quickly with time on stream at temperatures beyond 700–720 °C. At a lower temperature (<700 °C), it was speculated that CH<sub>4</sub> dissociation rate might be slower than carbon diffusion and carbon deposition rates. The unbalanced rates cause catalyst deactivation. Fragmentation and phase separation on NiCu particles occurred during the growth of CNTs, which caused further enrichment of carbon on the particle surface. Similar observations were also reported over NiCu/CNT catalysts with different metal ratios by Lua and co-workers.<sup>30,31</sup> Ni separation from the NiCu alloy particles mainly resulted in the deactivation at lower temperatures (<700 °C), whereas fragmentation of the alloy particles contributed to the deactivation with time on stream at higher temperature (>700 °C). In a recent study of NiCu catalysts on different supports (MgO or Al<sub>2</sub>O<sub>3</sub>), Cu doping was found to affect the lattice constants and particle size distribution of a solid solution Ni<sub>x</sub>Cu<sub>(1-x)</sub> which affect catalytic activity and stability.<sup>24</sup>

The quality of the carbon products is also critical to the commercialization of the TCD process. Techno-economic assessments emphasize that the cost of H<sub>2</sub> production depends strongly on the recovery and sale of solid carbon products.<sup>48</sup> Examples of valuable carbon products are graphitic carbon, carbon nanotubes and carbon nanofibers.<sup>48,49</sup> Formation of the carbon product is also affected by catalyst properties (*e.g.*, composition, support, crystalline structure, size of active metal particles) and operating conditions (*e.g.*, temperature, pressure, composition of gas feedstock).<sup>9,24,50</sup> For instance, a mixture of carbon-encapsulated metal particles, carbon filaments with different diameters and bamboo-shaped carbon were produced on a NiCu/Al<sub>2</sub>O<sub>3</sub> catalyst.<sup>25</sup> Selective formation of the bamboo-shaped carbon tubes was achieved under certain conditions (Cu loading, reaction temperature, composition of gas feedstock). Ultimately, the desirable carbon properties (*e.g.*, I<sub>D</sub>/I<sub>G</sub> ratio) would be dictated by the end use application(s). However, we lack quantitative evaluations the relationship of carbon properties to catalyst design parameters.

Here, we investigate the role of Cu in 1) catalytic performance (stability and activity) and 2) properties of carbon co-products. In particular, we evaluated the role of Ni/Cu ratio, reaction temperature, and synthesis protocol. We characterized the fresh and spent catalyst *via* X-ray diffraction (XRD), Raman Spectroscopy, and Scanning Transmission Electron Microscopy (STEM) to correlate trends in catalytic performance with changes in catalyst properties during reaction.

## Materials and methods

### Materials and catalyst synthesis

Nickel nitrate hexahydrate (Ni(NO<sub>3</sub>)<sub>2</sub>·6H<sub>2</sub>O), copper nitrate hemi-pentahydrate (Cu(NO<sub>3</sub>)<sub>2</sub>·2.5H<sub>2</sub>O), acetone and concentrated nitric acid (HNO<sub>3</sub>) were purchased from Sigma Aldrich. Multiwalled CNTs with outer diameter 20–30 nm



were provided by Cheap Tubes (<https://www.cheaptubes.com/>, catalog number 030104).

### Preparation of NiCu<sub>x</sub>/CNT catalysts *via* the solvothermal (ST) method

We prepared a series of NiCu<sub>x</sub>/CNT catalysts, where *x* represents the targeted weight loading of Cu, following the solvothermal (ST) method we have reported elsewhere.<sup>35</sup> The Ni loading was kept constant at approximately 10 wt% and the Cu wt% loading was varied to target a loading of 0 to 15 wt%. In the typical ST synthesis of a 10 wt% Ni-1 wt% Cu on CNT (NiCu1/CNT (ST)), 0.347 g of Ni(NO<sub>3</sub>)<sub>2</sub>·6H<sub>2</sub>O and 0.0154 g of Cu(NO<sub>3</sub>)<sub>2</sub>·2.5H<sub>2</sub>O were first dissolved in 60 mL acetone and sonicated for 30 min. As-received CNT (0.626 g) was added to the acetone solution and sonicated for additional 30 min. The mixture was then transferred into a 100 mL Teflon-lined Parr reactor, sealed, and stirred for 30 min. The Parr reactor was heated to 120 °C and maintained at this temperature for 12 h under static condition. After cooling to room temperature, the solution was retrieved from the Parr reactor, placed in a glass container, and allowed to evaporate overnight at room temperature and atmospheric pressure in a hood. The dry solids were placed in a furnace with stagnant air at 80 °C overnight. The dry solids were then crushed and sieved (100 mesh) and stored in a glass vial.

### Preparation of NiCu1 catalysts *via* incipient wetness (IW) and sequential impregnation (SI) methods

**Preparation of acid-treated CNT (HCNT) as support material.** The CNT was acid treated to functionalize its surface and allow for a better distribution of the metal during impregnation.<sup>51,52</sup> In a typical acid treatment, 3 g of as-received CNT was suspended in 150 mL 10 M HNO<sub>3</sub> solution and sonicated for 30 min. The solution was then placed in a reflux apparatus heated with an oil bath set at 100 °C for 14 h. Once the system cooled to room temperature, the solution was filtered to recover the solid, which was washed with copious distilled water until the pH of the filtrate was around 7. The acid-washed products were dried at 60 °C in a furnace with stagnant air for 12 h. The dried, acid-washed CNT (HCNT) were cooled and stored in a glass vial.

**Preparation of catalyst *via* co-impregnation (CI) and sequential impregnation (SI).** The catalyst synthesized by co-impregnation were prepared by mixing a 46 mL aqueous solution containing Ni(NO<sub>3</sub>)<sub>2</sub>·6H<sub>2</sub>O (0.7331 g) and Cu(NO<sub>3</sub>)<sub>2</sub>·2.5H<sub>2</sub>O (0.0570 g) with 1.3 g HCNT. The mixture was sonicated for 30 min and stirred for 2 h at room temperature. Then, the solvent was allowed to evaporate at ambient conditions in a ventilated hood. Once dry, the solids were heat treated: first dried in air at 140 °C for 8 h and then 1.72 g were heated to 350 °C at a ramp rate of 5 °C min<sup>-1</sup> in a N<sub>2</sub> and held at 350 °C for 3 h. Once cooled to room temperature, the treated solids were stored in a capped glass vial. The catalyst synthesized by this method are denoted as NiCu1/HCNT (CI).

The sequential-impregnated catalysts followed the same protocol as the co-impregnated catalysts (0.771 g Ni(NO<sub>3</sub>)<sub>2</sub>·6H<sub>2</sub>O, 0.0570 g Cu(NO<sub>3</sub>)<sub>2</sub>·2.5H<sub>2</sub>O), but only impregnating one metal at the time and heat treating after each impregnation. The catalyst was first impregnated with Ni followed by Cu impregnation and is denoted as Cu1Ni/HCNT (SI).

**Preparation of incipient wetness catalysts NiCu1/HCNT(IW).** The catalyst synthesized by incipient wetness impregnation (IW) were prepared by slowly adding a concentrated aqueous solution of Ni(NO<sub>3</sub>)<sub>2</sub>·6H<sub>2</sub>O (0.595 g) and Cu(NO<sub>3</sub>)<sub>2</sub>·2.5H<sub>2</sub>O (0.0439 g) to HCNT (1.068 g) using the amount of liquid that was previously determined to just wet the support (0.595 mL g<sup>-1</sup>). Then, the slurry was dried in a furnace under stagnant air at 80 °C overnight. Once dry, the solids were then heated in air at 140 °C for 8 h followed by heating 500 mg in flowing N<sub>2</sub> (30 cm<sup>3</sup> min<sup>-1</sup>) of at 350 °C for 3 h. The temperature ramp rate was 5 °C min<sup>-1</sup>. Once cooled to room temperature, the solids were stored in a capped glass vial. The nominally 10 wt% Ni and 1 wt% Cu catalyst prepared by IW is denoted as NiCu1/HCNT (IW).

### Characterization

The catalysts were characterized before (fresh) and after reaction (spent) to determine their stability and to devise relationships between activity, stability, and surface properties. The 500 mg of fresh catalysts were reduced at 400 °C for 4 h under 30 cm<sup>3</sup> min<sup>-1</sup> of 5 vol% H<sub>2</sub> in N<sub>2</sub> followed by heating to reaction temperature (typically 600 °C) in 30 cm<sup>3</sup>/min N<sub>2</sub>. After cooling to room temperature, the samples were passivated by flowing (30 cm<sup>3</sup> min<sup>-1</sup>) 1 vol% O<sub>2</sub> in N<sub>2</sub> overnight. The spent catalysts were characterized as retrieved from the TCD reactor.

Nitrogen (N<sub>2</sub>) physisorption of the fresh and spent catalysts was conducted on a Quadrasorb EVO/SI Gas Sorption System from Quantachrome Instruments at 77 K. Samples were degassed at 150 °C under vacuum for 12 h. Surface areas were determined using the 5-point Brunauer-Emmett-Teller (BET) method from the adsorption data in the relative pressure range of 0.05–0.3. Metal loadings were determined by inductively coupled plasma optical emission spectrometry (ICP-OES).

XRD patterns were collected using a Rigaku SmartLab SE Bragg-Brentano diffractometer, equipped with a fixed Cu anode operated at 40 kV and 44 mA and a D/Tex Ultra 250 1-dimensional detector. Patterns were collected with a variable divergence slit between 2 and 100° (2θ) at intervals of 0.01°. The composition present, lattice parameters, and crystallite sizes of the crystalline components were determined by Rietveld fitting between 30 and 100° (2θ) using Topas v6 (Bruker AXS) as discussed elsewhere.<sup>53</sup> Because of the presence of NiCu alloys containing a range of compositions, we acknowledge that this method could underestimate the crystallite size. The compositions of the metallic phases were estimated from their refined cubic



lattice parameters by linear interpolation between Ni ( $a = 3.5238 \text{ \AA}$ ) and Cu ( $a = 3.615 \text{ \AA}$ ).

A Micromeritics AutoChem 2920 instrument was used to conduct temperature programmed oxidation (TPO). The samples were first loaded and pretreated at  $120 \text{ }^\circ\text{C}$  for 120 min under He, and then heated to  $800 \text{ }^\circ\text{C}$  at a ramp rate of  $5 \text{ }^\circ\text{C min}^{-1}$  under 5 vol%  $\text{O}_2$  in He.

Raman spectra were recorded on a Renishaw InVia Raman microscope with a 532 nm excitation wavelength at 10 mW laser power. Each spectrum was averaged over three scans to characterize the solid carbon co-produced by  $\text{CH}_4$  TCD.

A FEI Titan 80–300 High-resolution transmission electron microscope (HRTEM) microscope operated at 300 kV and equipped with a CEOS GmbH double-hexapole aberration corrector for the probe-forming lens, energy-dispersive X-ray (EDX) spectroscopy detector was used to determine the morphology of solid carbon co-products, metal particle size, and element distribution before and after reaction. Metal particle size and composition distributions were calculated from HRTEM images by sampling an average of 100 particles.

### Catalytic tests

A fixed-bed, continuous-flow, vertical stainless-steel reactor was used for  $\text{CH}_4$  TCD reaction at ambient pressure, as detailed in our previous work.<sup>53</sup> As-synthesized catalysts (0.2 g, assumed density =  $0.33 \text{ g cm}^{-3}$ ) were loaded between two plugs of quartz wool.  $\text{N}_2$  gas was used as a carrier gas and an internal standard for product analysis using on-line gas chromatography (GC). Prior to each test, the 0.2 g catalyst samples were reduced *in situ* at  $400 \text{ }^\circ\text{C}$  for 4 h under  $70 \text{ cm}^3 \text{ min}^{-1}$  10 vol%  $\text{H}_2$  in  $\text{N}_2$  at a ramp rate of  $3 \text{ }^\circ\text{C min}^{-1}$ . Subsequently, the reactor was heated to the reaction temperature (*i.e.*,  $550$  to  $700 \text{ }^\circ\text{C}$ ) under  $70 \text{ cm}^3 \text{ min}^{-1}$  of  $\text{N}_2$ . Before reaction, we checked that the  $\text{H}_2$  had been completely purged from the system (monitored by on-line GC). Then, the feed was switched to  $30 \text{ cm}^3 \text{ min}^{-1}$  of 30 vol%  $\text{CH}_4$  in  $\text{N}_2$  to maintain a constant space velocity of  $9000 \text{ cm}^3 \text{ g}^{-1} \text{ h}^{-1}$  ( $\approx 3000 \text{ h}^{-1}$  at the assumed density of the bed). The outlet gas flow rate was measured by a digital flow meter (DryCal). Composition of the outlet gas was analyzed by a four-channel Agilent Micro GC equipped with Molecular Sieve 5A, PLOT U, alumina, and OV-1 columns and a TCD detector for each column. When the test concluded, the reactor system was cooled to room temperature under  $30 \text{ cm}^3 \text{ min}^{-1}$  of  $\text{N}_2$ , and the spent catalysts (containing solid carbon co-product) were retrieved from the reactor for analysis.  $\text{H}_2$  was the only gaseous reaction product,  $\text{CO}_2$  and  $\text{CO}$  were not detected.

$\text{CH}_4$  conversion,  $X_{\text{CH}_4}$ , was calculated based on the amount of  $\text{CH}_4$  reacted shown in eqn (1):

$$X_{\text{CH}_4}(t)/\% = \frac{F_{\text{In}} \cdot [\text{CH}_4]_{\text{In}} - F_{\text{Out}} \cdot [\text{CH}_4]_{\text{Out}}}{F_{\text{In}} \cdot [\text{CH}_4]_{\text{In}}} \cdot 100 \quad (1)$$

where  $F_{\text{In}}$  is the flow rate of the feed gas determined by DryCal before reaction starts;  $[\text{CH}_4]_{\text{In}}$  is the concentration of

$\text{CH}_4$  in the feed gas determined by GC;  $F_{\text{Out}}$  is the flow rate of the outlet gas determined by DryCal;  $[\text{CH}_4]_{\text{Out}}$  is the concentration of  $\text{CH}_4$  in the outlet gas determined by GC.

Carbon yield  $Y_{\text{C}}(t)$  and the rate of deposition of carbon were calculated as the accumulated weight of carbon per mass of the catalyst based on the  $\text{CH}_4$  conversion. Typically, the reactions were run for over 14 h or until we achieved total carbon yields of  $3.5 \text{ g}_{\text{carbon}}/\text{g}_{\text{catalyst}}$  (*i.e.*,  $>80\%$  of the carbon in the spent catalysts was carbon co-product). That accumulation ensured that the characterization of the spent catalyst was representative of the carbon co-product instead of the starting carbon support.

The mole balance of the results reported in this work was between 95 and 100% and was calculated using eqn (2):

$$\text{Mole Balance, \%} = \frac{F_{\text{Out}} \times \left( [\text{CH}_4]_{\text{Out}} + \frac{[\text{H}_2]_{\text{Out}}}{2} \right)}{F_{\text{In}} \times [\text{CH}_4]_{\text{In}}} \times 100 \quad (2)$$

## Results and discussions

### Performance of $\text{NiCu}_x/\text{CNT}$ (ST) catalysts with different bulk Cu compositions

A series of  $\text{NiCu}$  catalysts synthesized by the solvothermal method (ST) with a constant 10 wt% Ni loading were tested at  $600 \text{ }^\circ\text{C}$  under  $30 \text{ cm}^3 \text{ min}^{-1}$  of 30 vol%  $\text{CH}_4$  in  $\text{N}_2$ . Cu loading was changed 0 to 15 wt% to probe the effect of Cu on the TCD activity and morphology of carbon co-product. The catalysts properties such as BET and ICP-derived metal content are summarized in Table S1.† The addition of Cu to

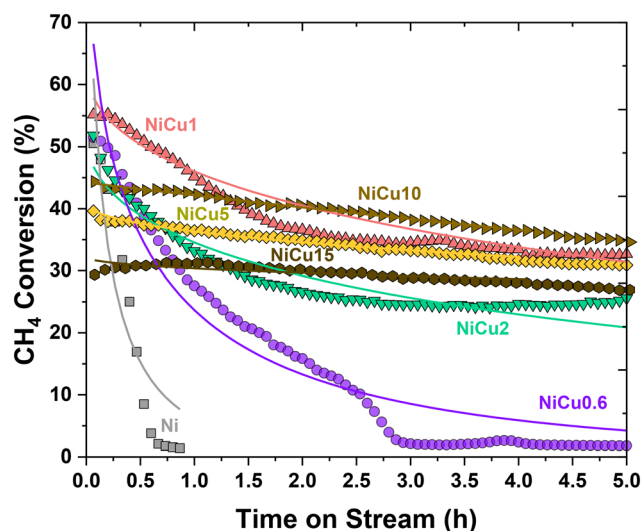


Fig. 1  $\text{CH}_4$  conversions at time on stream for  $\text{NiCu}_x/\text{CNT}$  ( $x = 0, 0.6, 1, 2, 5, 10, 15$ ) catalysts prepared by solvothermal method at reaction temperature of  $600 \text{ }^\circ\text{C}$  under  $30 \text{ cm}^3 \text{ min}^{-1}$  30 vol%  $\text{CH}_4$  in  $\text{N}_2$ . The background activity of the CNT support was  $<0.2\%$   $\text{CH}_4$  conversion. The carbon yield and carbon deposition rate as a function of time on stream can be found in Fig. S2.† The lines represent a decaying exponential fit and the fitting parameters are shown in Table 1.



**Table 1** Fitting parameters for deactivation at 600 °C and the actual (*i.e.*, experimental) and predicted carbon yield at the indicated time on stream,  $\theta$ . The catalyst sample weighed 0.2 g so all but three samples (Ni/CNT (ST), NiCu0.6/CNT (ST), and NiCu1/HCNT (CI)) accumulated an amount of carbon that exceeded the mass of the MWCNT support (*i.e.*, <0.18 g) at the indicated, final time on stream

Catalyst	Cu mol fraction	$X_0$ (%)	$k$ ( $\text{h}^{-0.5}$ )	$\theta$ (h)	Actual carbon yield ( $\text{g}_\text{C}/\text{g}_{\text{cat}}$ )	Predicted carbon yield ( $\text{g}_\text{C}/\text{g}_{\text{cat}}$ )
Ni/CNT (ST)	0	135	3.09	0.87	0.282	0.251
NiCu0.6/CNT (ST)	0.045	97	1.17	5.00	0.957	1.02
NiCu1/CNT (ST)	0.081	63	0.309	5.00	2.52	2.61
NiCu2/CNT (ST)	0.142	48	0.333	5.00	1.89	1.88
NiCu5/CNT (ST)	0.35	41	0.120	5.00	2.23	2.24
NiCu10/CNT(ST)	0.455	47	0.110	5.00	2.59	2.63
NiCu15/CNT (ST)	0.553	32	0.0561	5.00	1.93	1.94
NiCu1/HCNT (IW)	0.086	53	0.760	5.00	1.21	1.19
NiCu1/HCNT (CI)	0.079	60	1.20	4.00	0.725	0.731
Cu1Ni/CNT (SI)	0.083	54	0.0800	5.00	3.15	3.13

Ni affects the initial TCD activity and stability (Fig. 1). For high loadings of (*i.e.*, nominal Cu loadings of 0, 0.6, 1.0 wt%), the earliest measurements of  $\text{CH}_4$  conversions remain similar to that of pure Ni (*i.e.*, 60%) but the catalyst stability is enhanced with increasing Cu. Catalysts with higher mole fractions of Cu (*i.e.*, nominal Cu weight loadings of 2, 5, 10, and 15 wt%) have lower initial TCD activity but deactivate much more slowly.

To approximately quantify the deactivation of the catalysts, we borrowed two ideas from the literature. First, we assumed that the carbon accumulated with time on stream,  $\theta$ , raised to a small power, *viz.*  $C \propto \theta^{0.5}$ , as postulated by Voorhies for catalytic cracking.<sup>54</sup> Second, we assumed that the catalyst deactivation could be represented through a poisoning factor,  $\Phi$ , that would multiply the initial rate of conversion,  $X_0$ :

$$X(\theta) = X_0 \times \Phi(C(\theta)) \quad (3)$$

Following an empirically motivated suggestion by Froment and Bischoff,<sup>55</sup> we assumed that  $\Phi(C)$  was simply a decaying exponential that depended on the accumulated carbon:

$$\Phi(C) = \exp(-kC) \quad (4)$$

Therefore, we fit the  $\text{CH}_4$  conversion as a function of time on stream using a functional form with two coefficients, the initial conversion,  $X_0$ , and a deactivation rate parameter,  $k$ .

$$X(\theta) = X_0 \times \exp(-k\theta^{0.5}) \quad (5)$$

Curves corresponding to the fitting parameters presented in Table 1 have been superposed on the data shown in Fig. 1 and 2. We also tried another empirical suggestion of Froment and Bischoff that the deactivation function was Langmurian,  $\Phi(C) = 1/(1 + kC)$ , but found that it fit the data poorly.

The properties of the Ni and Cu metal in freshly reduced catalysts were investigated with XRD (Fig. S1†) to understand the roles that Cu played in the TCD performance and results are summarized in Table S2.† The freshly reduced NiCu catalysts are mainly composed of reduced NiCu alloy

nanoparticles. The catalysts with Ni/Cu mass ratios >5 had larger nanoparticles (*e.g.*, 11–14 nm) compared to the catalyst with Ni/Cu mass ratio <2 (*e.g.*, 7.3 to 8.6 nm). In our previous work we showed the crystallite size of monometallic Ni nanoparticle is the dominant factor for TCD activity,<sup>53</sup> which also coincides with the activity trends discussed in this work. That is, catalysts with high Ni/Cu mass ratios (*i.e.*, >5) yield metal nanoparticles with larger particle size and higher TCD activity. On the other hand, catalysts with low Ni/Cu mass ratios (*i.e.*, <2) yield smaller metal nanoparticles with lower TCD activity. This relationship between TCD activity and NiCu crystallite size is also consistent with previous reports by Pinilla *et al.*<sup>24</sup> The Ni/Cu ratios derived from XRD are different from the ones obtained *via* ICP specially at high Ni/Cu ratios (*i.e.*, >5); we infer that the XRD analysis might be excluding some particles from the analysis or

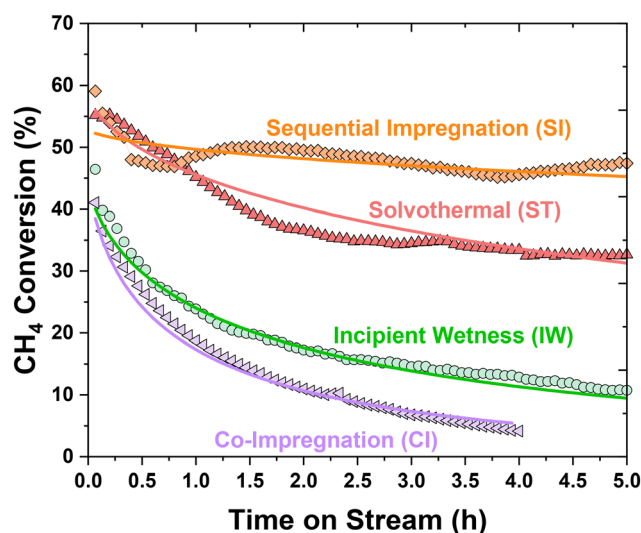


**Fig. 2** Activity of NiCu1/CNT prepared by different synthesis methods as a function of time on stream at reaction temperature of 600 °C under  $30 \text{ cm}^3 \text{ min}^{-1}$  30 vol%  $\text{CH}_4$  in  $\text{N}_2$ . GHSV  $\approx 3000 \text{ h}^{-1}$ . The background activity of the raw CNT was <0.2%  $\text{CH}_4$  conversion. The carbon yield and carbon deposition rate as a function of time on stream can be found in Fig. S2.† The lines represent a decaying exponential fit and the fitting parameters are shown in Table 1.



underestimating the metal compositions. However, we speculate that the enhanced TCD stability of the catalysts with <2 Ni/Cu ratio might be a direct result of the higher Cu loadings used in the catalysts.

The spent catalysts were also analyzed *via* XRD to elucidate the role of Cu on catalyst stability and the results are shown in Table S2.† Overall, we observed changes in both crystallite size and re-distribution of metal compositions. All but one of the catalysts showed a loss of Ni on the alloy (*i.e.*, Ni/Cu ratio decreased), most likely resulting from the selective Ni migration from the metal particles to the carbon co-product. The segregation of Cu and Ni from the different Ni/Cu alloy nanoparticles at the reaction temperatures is consistent with the solubility gap regions of the NiCu phase diagram.<sup>56</sup> Out of the 7 different Ni/Cu catalysts evaluated, only NiCu1 underwent particle fragmentation as evidenced by the 15% decrease in average crystallite size. The other six catalysts underwent metal sintering as evidenced by the average crystallite size increase between 7% and 100%, Table S2.† Hence, we speculate that the changes in TCD catalytic performance depicted in Fig. 1 are a result of both the changes in Ni/Cu ratio and average crystallite size of the active site, which is also consistent with previous works by Shen *et al.* and Adeeva *et al.*<sup>30,31</sup>

### Effect of synthesis method on TCD catalytic performance

Catalysts with the same nominal weight loadings of 10 wt% Ni and 1 wt% Cu were prepared using different synthesis methods to investigate the effect on metal particle size, Ni/Cu composition, and catalytic performance; solvothermal deposition (ST), incipient wetness impregnation (IW), wet co-impregnation (CI), and wet sequential impregnation (SI). The synthesis method affected the CH<sub>4</sub> conversion and catalyst stability (Fig. 2). The catalyst synthesized by both the ST and SI methods had the highest activity and stability compared to the catalyst synthesized by IW and CI. Table S3† summarizes the characterization of the fresh catalysts and shows that while all the catalysts had similar Ni/Cu ratios, the weight loadings varied up to 47% with respect to the ST catalyst. Fig. S2† show that when accounting for the differences in metal content, the catalysts synthesized by the ST method had the highest TCD activity (*i.e.*, carbon deposition rate and carbon yield). ICP revealed that all the catalysts had similar Ni/Cu ratios (10.7 to 11.8); however, XRD analysis shows that the Ni/Cu ratio on the metal particles ranged from 13.0 to 24.3 while the metal particle size remained similar between 8.0 and 11 nm. These results suggest that the synthesis method of the freshly reduced samples affected primarily the distribution of Ni and Cu on the metal nanoparticles and not the metal particle.

XRD analysis of the spent catalysts revealed an even larger variation in Ni/Cu ratios (19 to 49). The catalysts synthesized by ST and SI methods had the lowest Ni/Cu ratios of 19 (each), while the catalysts prepared by IW and CI had significantly higher Ni/Cu ratios of 32 and 49 (Table S3†). The ST and SI

catalysts also had the lowest deactivation rate constants of 0.42 and 0.08. In contrast, the catalysts prepared by IW and CI had higher deactivation rate constants of 0.76 and 1.2 (Table 1). Thus, catalysts composed of bimetallic NiCu metal nanoparticles with significantly higher Cu contents (smaller Ni/Cu ratios) were more stable. Further, while XRD analysis showed that metal particle size increased after reaction for three of the four catalysts, the catalyst prepared by SI had the largest particle size (15.1 nm) and also exhibited the largest increase in growth (from 8.4 nm). This combination of large particle size and low Ni/Cu ratio, compared to the other catalysts, could explain its superior stability. Taken together, the XRD analysis of the spent catalysts reveals that the particle size and Ni/Cu ratio changed with the synthesis method, and this can directly explain differences in catalytic stability.

### Effect of reaction temperature on TCD catalytic performance

We evaluated the performance of three catalysts [Ni/CNT (ST), NiCu1/CNT (ST), and NiCu15/CNT (ST)] as a function of reaction temperature (550–700 °C). Fig. 3 shows how the Ni/Cu composition affects the TCD activity and stability at different reaction temperatures. For example, at 550 °C, pure Ni catalysts showed the highest CH<sub>4</sub> conversion compared to NiCu1 and NiCu15 and slow deactivation during 4 h. Increasing the reaction temperature for the pure Ni system to 600 °C caused nearly complete catalyst deactivation within 1 h. However, the catalyst containing 1 and 15 wt% Cu remained stable at 600 °C even though the CH<sub>4</sub> conversion was inversely proportional to the Cu content. At 650 °C both pure Ni/CNT and NiCu1/CNT catalysts deactivated within 1 h while NiCu15 remained stable for >4 h. At 700 °C both Ni and NiCu1 deactivated within 15 min of reaction while NiCu15 exhibits a slower deactivation and lasted for nearly 2 h. Hence, these results suggest that the addition of Cu is detrimental to the TCD catalytic activity at operation temperatures <550 °C, while the addition of Cu is beneficial at temperatures ≥600 °C.

Given the assumed functional form for the deactivation function, the mass of carbon at any time on stream,  $C(\theta)$ , is easily estimated by integrating eqn (5) multiplied by the inlet hourly mass flow rate of carbon,  $C_{\text{feed}}$  and the initial, fitted conversion,  $X_0$

$$C_{\text{feed}} = \frac{30 \frac{\text{cm}^3}{\text{min}} \times \left( \frac{30 \text{ vol}\% \text{ CH}_4}{100} \right) \times 60 \frac{\text{min}}{\text{h}} \times 0.987 \text{ atm}}{1000 \frac{\text{cm}^3}{\text{L}} \times (0.0821 \frac{\text{L atm}}{\text{mol K}}) \times 298 \text{ K}} \quad (6)$$

$$\times \frac{1 \text{ mol C}}{1 \text{ mol CH}_4} \times \frac{12 \text{ g C}}{1 \text{ mol C}} = 0.262 \text{ g}_c \text{ h}^{-1}$$

$$C(\theta) = C_{\text{f}} X_0 \int_0^\theta \exp(-k\theta^{0.5}) d\theta$$

$$= -C_{\text{f}} X_0 \frac{2e^{(-k\theta^{0.5})} (k\theta^{0.5} + 1)}{k^2} \Big|_0^\theta \quad (7)$$

The predicted amount of carbon co-product accumulated (*i.e.*, carbon yield) closely tracked the actual amount of



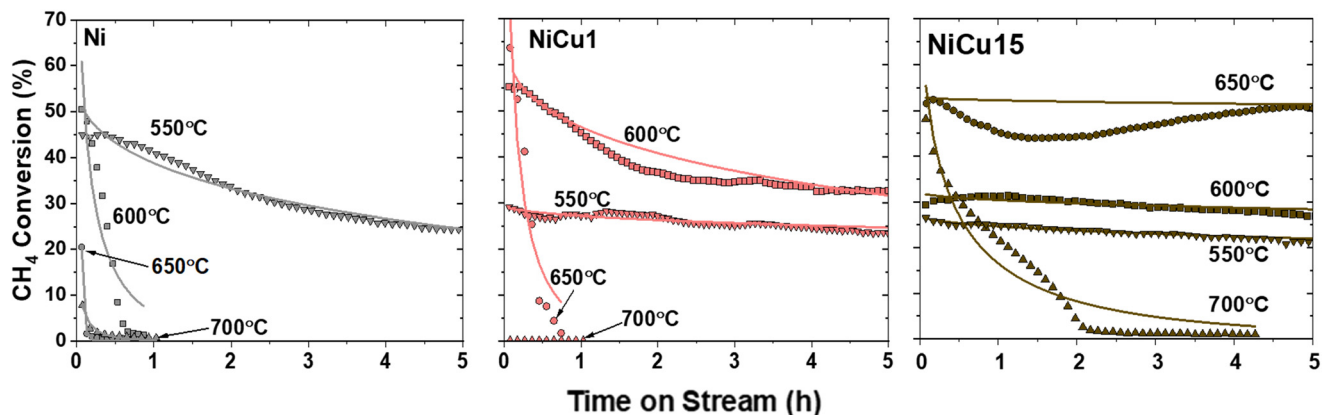


Fig. 3 Activity of Ni/CNT (ST), NiCu1/CNT (ST), and NiCu15/CNT (ST) as a function of time on stream at reaction temperatures of 550–700 °C under 30 cm<sup>3</sup> min<sup>-1</sup> 30 vol% CH<sub>4</sub> in N<sub>2</sub>. The background activity of the raw CNT was <0.2% CH<sub>4</sub> conversion and was ignored in the curve fitting. The fitting parameters can be found in Table S4.†

carbon measured in the reactor (Fig. 4), lending credence to the chosen functional form. On the basis of the adequate fits of both the instantaneous and the integral conversion, we have calculated the projected carbon yield extrapolated the accumulation of carbon co-product to  $\theta = \infty$  normalized by the weight of catalysts:

$$\text{Projected Carbon Yield} = \frac{C(\infty)}{\text{Cat. Weight}} = \frac{2 \times C_f \times X_0}{\text{Cat. Weight} \times k^2} \quad (8)$$

Those values exhibit a maximum that depends on both the operating temperature and catalyst composition, represented by the mol fraction of Cu (Fig. 5). These results are consistent with previous reports detailing the effect of Cu addition on Ni TCD activity.<sup>27–31</sup> The carbon accumulation shows that there is an optimum in Ni/Cu ratio at each operating temperature.

The spent catalysts were analyzed *via* XRD to elucidate the role of Cu on catalyst stability. The results show that metal particle restructuring might have caused catalyst deactivation at the different reaction temperatures. For example, as shown in Table S3† the metal particles in Ni/CNT remained small at 9.2 nm when operating at 550 °C but sintered to larger metal particle sizes (14.6 to 19.4 nm) when the reaction temperature increased, suggesting that a cause of deactivation was metal sintering. NiCu1/CNT maintained small metal particle sizes and TCD activity at 550 and 600 °C, which is consistent with the small change in metal particle size and Ni/Cu ratio observed with respect to the fresh material. However, NiCu1 deactivated at 650 °C in less than 1 h while the metal particles sintered and segregated Cu into a secondary Cu-rich alloy. At 700 °C, NiCu1 was not active for

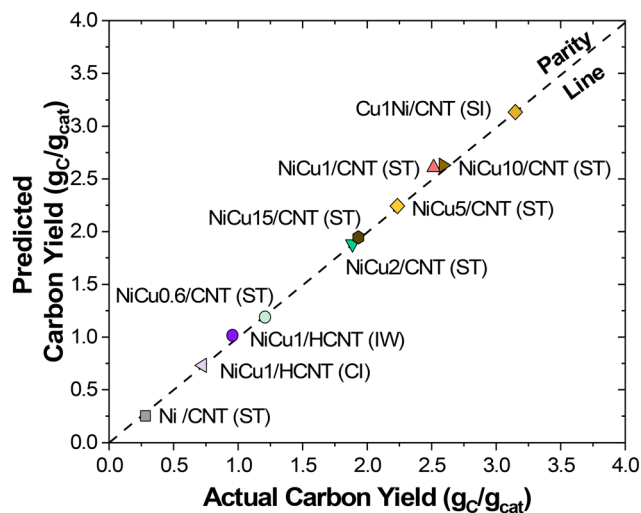


Fig. 4 Parity plot of carbon yield calculated as the predicted or actual accumulated carbon co-product normalized by the weight of catalyst used at the time on stream shown in Table 1.

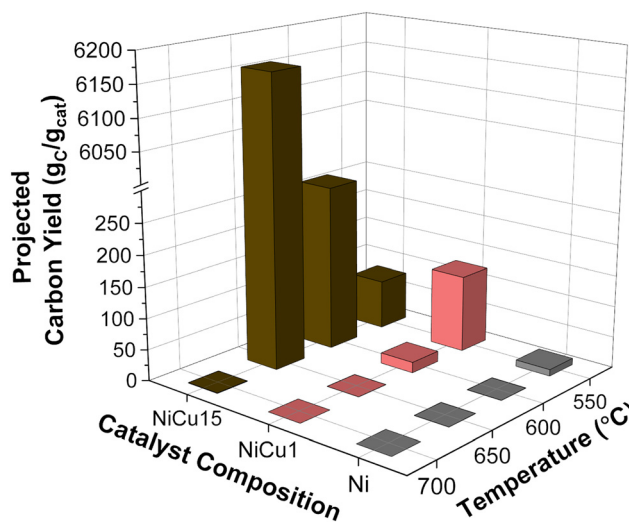


Fig. 5 Projected carbon yield calculated as projected carbon co-product accumulation of carbon at infinite residence divided by the weight of catalyst used according to eqn (8) as a function of the catalyst composition and operating temperature for catalysts prepared by the solvothermal (ST) method.





TCD and the composition and particle size remained similar to that of the fresh catalyst, suggesting that the catalyst deactivated before metal restructuring occurred.

We speculate that the deactivation at higher temperatures might be caused by selective formation of graphitic carbon and subsequent plugging of the active site as we previously reported.<sup>57</sup> Interestingly, NiCu15/CNT catalyst had similar metal particle size (17.2 to 21.4 nm) at 550, 600, and 650 °C for which the catalyst was active and stable; however, the Ni/Cu ratio of the metal particles changed with reaction condition. These results suggest there was a preferential segregation of Ni out of the metal particle at 550 °C by the change in Ni/Cu ratio with respect of the fresh catalyst (0.133 and 0.790 respectively). At 600 and 650 °C, the Ni/Cu ratio increased (0.254 and 0.418) suggesting that the segregation of Ni was less at higher reaction temperatures. At 700 °C, the Ni/Cu ratio of the metal particles was similar to that of the fresh catalyst (0.676 and 0.790), further corroborating that the Ni segregation is less at higher temperatures; however, the metal particle size only stabilized to 10.4 nm (from 8.60 nm on the fresh catalyst) as opposed to the larger metal particle size observed at the lowest temperatures. We speculate that the slow deactivation at 700 °C was caused by the poisoning of active sites before they could stabilize to the preferential particle morphology (*i.e.*, <0.254 Ni/Cu ratio and >17 nm). Hence, these results suggest that the role of Cu is to stabilize large metal particles (>17 nm); however, increasing the reaction temperatures cause metal migration and changes the Ni/Cu ratio below the required to stabilize the large metal particles. The properties of the carbon co-product form might also play a role on the catalyst stability, which is explored in the following section.

### Effect of Ni/Cu ratios on carbon co-product properties

As shown in Fig. S1,† XRD of the catalyst run at 600 °C reveals that the graphitic carbon features increase as the Ni and NiCu alloy metal features decrease corroborating the deposition of carbon. TPO of the spent samples run at 600 °C shows the deposited carbon co-product was mainly composed of crystalline carbon with oxidation temperatures was between 400 and 500 °C as opposed to amorphous carbon which typically oxidizes at 200–350 °C.<sup>53,58</sup> The oxidation temperature of the commercial (raw) MWCNT decreases from 500–550 °C to 200–250 °C upon the additional of NiCu bimetallic metal nanoparticles (*i.e.*, fresh NiCu<sub>x</sub>/CNT), suggesting that the bimetallic particles are catalyzing the oxidation reaction. However, the spent NiCu<sub>x</sub>/CNT materials exhibited oxidation temperatures between 400 and 450 °C (in the presence of bimetallic nanoparticles), suggesting that the CNT formed during the TCD reaction have higher thermal stability than the commercial CNTs used in this work as support. While the presence of monometallic 10 wt% Ni lowered the oxidation temperature of the spent material with respect to raw MWCNT by ≈50 °C, the addition of up to 15 wt% Cu to 10 wt% Ni further lowered the oxidation temperature by an additional ≈50

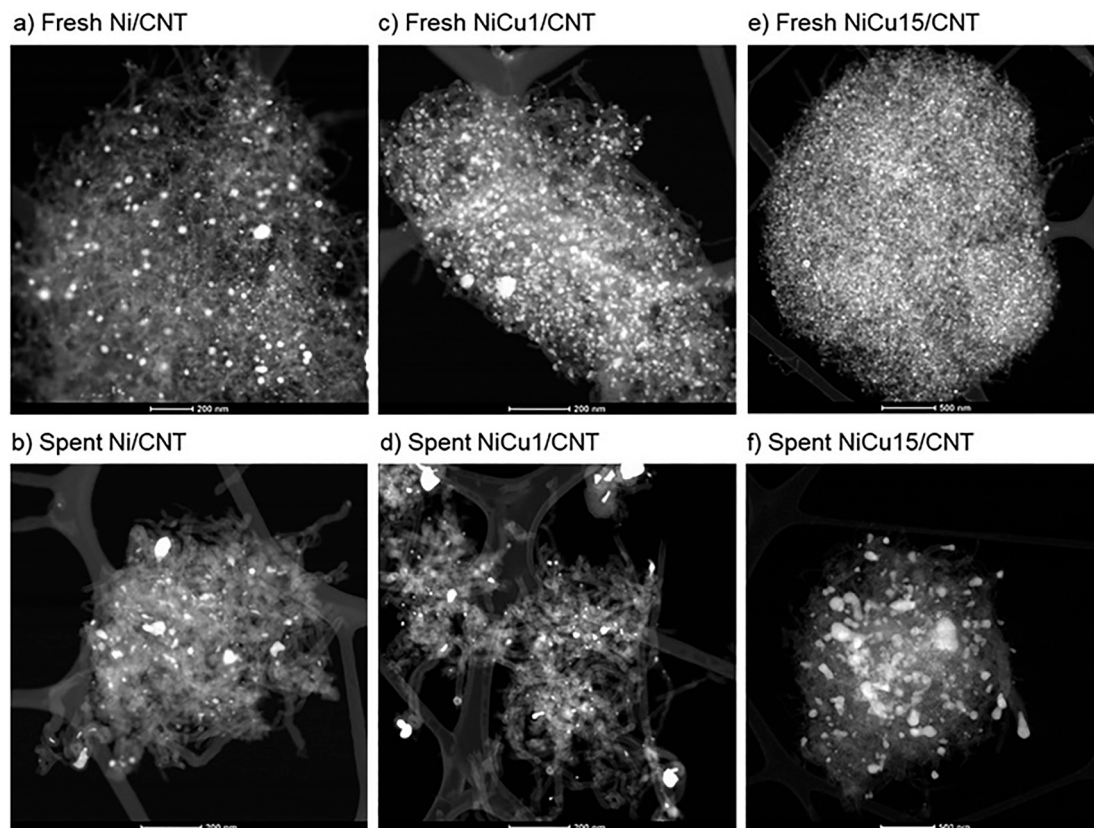
°C. We speculate this is caused by the increase in metal content that can catalyze the oxidation reaction at lower temperatures as opposed to a change in carbon co-product composition.

Fig. 6 shows the STEM images of selected samples after reaction at 600 °C revealing the selective formation of CNT as carbon co-product as well as the morphology and size of the metal particles. Overall, all the fresh catalysts are composed of a wide range of metal particles between 10 and 20 nm as XRD suggested; however, we found that the spent catalyst was composed of larger >50 nm (as well as <20 nm) particles for the three different compositions, which suggests that metal sintering took place during the TCD reaction. The XRD analysis summarized in Table S2† also showed metal particle sintering but did not capture the formation of the larger metal nanoparticles. We speculate that the larger metal nanoparticles observed by STEM are domains of multiple smaller crystals, which explains why the XRD analysis did not fully capture them. Fig. S6 and S5† are EDS maps of the catalyst after reaction and show that Ni and Cu remain in the metal particle regardless of the metal particle size; however, there appear to be changes in the Ni/Cu ratios of the spent materials and formation of Ni-rich and Cu-rich particles as revealed by the XRD analysis. More importantly, the HAADF STEM micrographs of the spent catalysts also reveal the selective formation of CNTs as the main solid co-product on the large metal nanoparticles. Fig. 7 shows the differences in morphologies of CNT produced by the different catalysts highlighting the role that Ni/Cu ratio played.

The addition of 1 wt% Cu (*i.e.*, NiCu1/CNT) produced multiwall CNT carbon co-product, which had a wall diameter ≈5 nm. Further increasing the Cu loading resulted in the formation of larger Ni/Cu metal particles, which generated large CNT with wall thickness >10 nm. Fig. S8 depicts more STEM images of spent NiCu15/CNT at 600 °C. The changes in carbon co-product morphology depicted in this work as a function of metal particle size is consistent with previous reports.<sup>25</sup>

As we previously showed,<sup>35</sup> Raman spectroscopy can be used to assess the carbon quality using the three main bands: a) D-band (1340 cm<sup>-1</sup>) associated with defects in the graphitic lattice,<sup>59,60</sup> b) G-band (1580 cm<sup>-1</sup>) associated with ordered carbon,<sup>59,60</sup> and c) G'-band (or 2D band, 2700 cm<sup>-1</sup>) associated with interactions between stacked graphene layers that can be used to distinguish between single-wall CNTs (SWCNTs) or multi-wall CNTs (MWCNTs).<sup>59,60,61</sup> Fig. 8 shows the  $I_D/I_G$  and  $I_{G'}/I_G$  ratios of the spent catalysts compared to the pristine support (MWCNT Support), pristine support run under reaction conditions, and fresh catalysts. The results reveal a direct correlation with the Ni/Cu ratio and the  $I_D/I_G$  and  $I_{G'}/I_G$  ratios of the generated CNT. For example, the  $I_D/I_G$  ratio was similar for the as received MWCNT (1.11) and MWCNT after exposed to reaction conditions (0.993) as well as the fresh catalysts (1.05 to 1.0); however, the spent catalysts showed a different  $I_D/I_G$  ratio suggesting that the CNT generated during TCD had different properties to that of the starting support. With the exception of Ni/CNT (ST) and NiCu1/HCNT (CI), the rest of the catalysts had a similar final carbon deposited per gram of catalyst (>4 g<sub>carbon co-product</sub>/





**Fig. 6** High-angle annular dark-field (HAADF) imaging using a scanning transmission electron microscope (STEM) of selected catalyst before (fresh) and after reaction (spent) at 600 °C under 30 cm<sup>3</sup> min<sup>-1</sup> 30 vol% CH<sub>4</sub> in N<sub>2</sub>. Associated elemental maps obtained with Energy-Dispersive Spectroscopy (EDS) can be found in Fig. S6 and S7.†

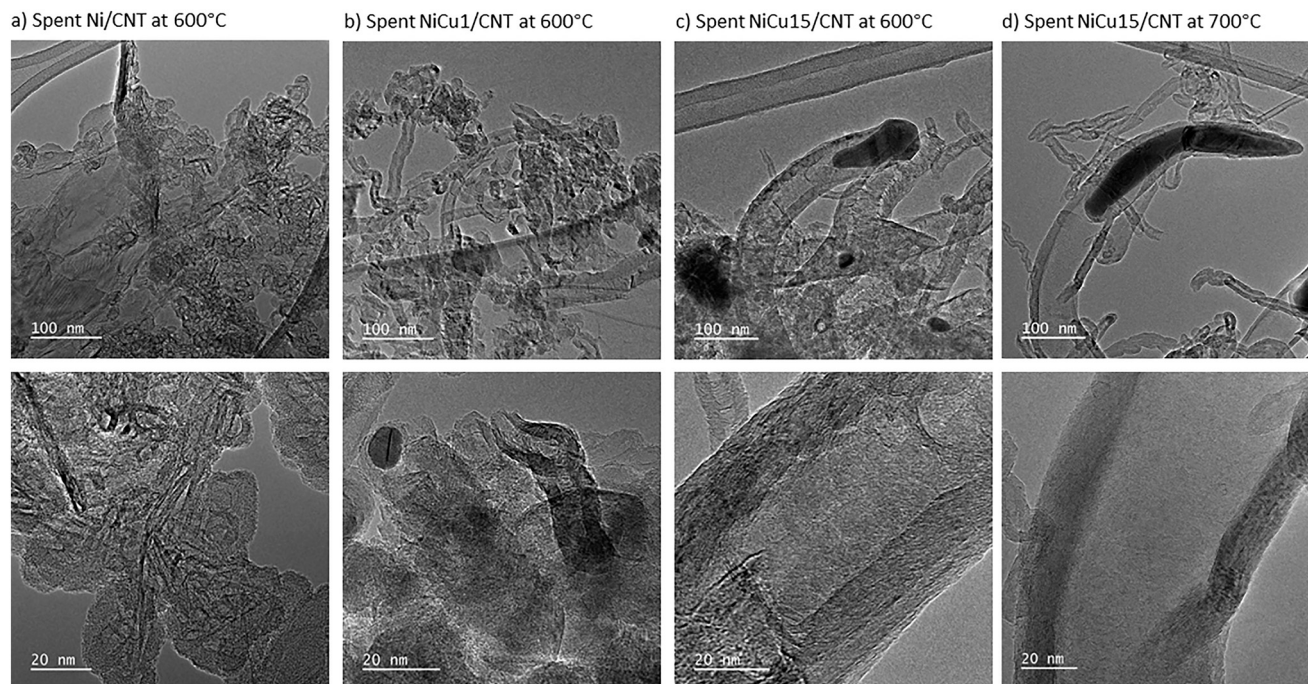


**Fig. 7** Scanning transmission electron microscope (STEM) images of selected catalyst after reaction (spent) at a–c) 600 °C and d) 700 °C under 30 cm<sup>3</sup> min<sup>-1</sup> 30 vol% CH<sub>4</sub> in N<sub>2</sub>. Additional STEM images can be found in Fig. S8 and S9.†

g<sub>carbon support</sub>); hence, the changes in  $I_D/I_G$  and  $I_G/I_G$  ratios as a function of Ni/Cu composition can be attributed to changes

in the morphology of the deposited carbon co-product. Ni/CNT was only active for 1 h at 600 °C and there was little



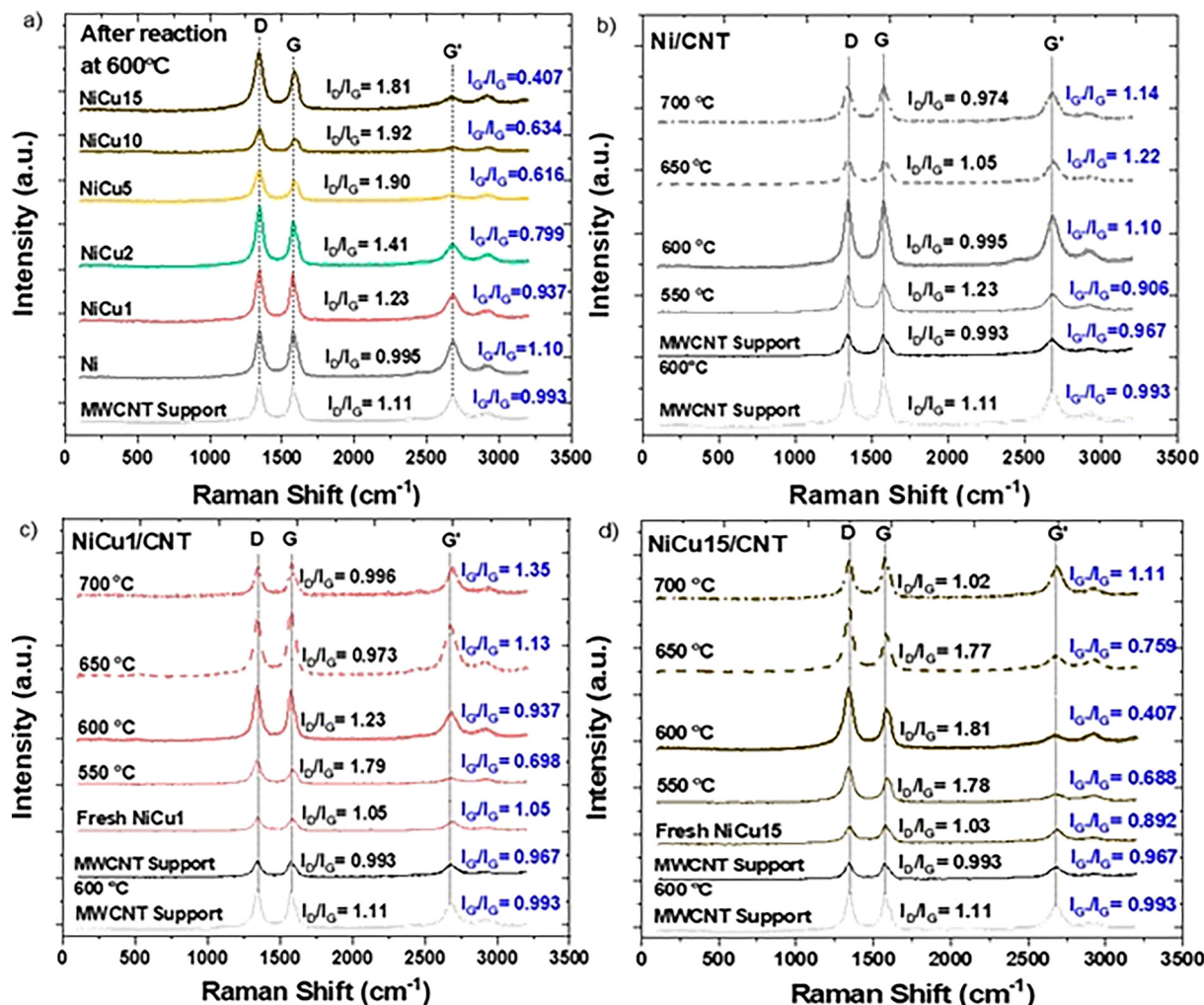


Fig. 8 Raman spectra of a) spent solvothermal (ST) catalysts with different Ni/Cu ratio run at 600 °C, b) Ni/CNT, c) NiCu1/CNT, and d) NiCu15/CNT run at different temperatures under 30 cm<sup>3</sup> min<sup>-1</sup> 30 vol% CH<sub>4</sub> in N<sub>2</sub>. The spectra were collected using a 10 mW laser at a 532 nm excitation wavelength. With the exception of Ni/CNT run at >600 °C, all the other catalyst run at 700 °C, and CNT support, >80% of the mass of the catalyst was composed of carbon co-product generated during TCD.

carbon deposited ( $\sim 1 \text{ g}_{\text{carbon co-product}}/\text{g}_{\text{carbon support}}$ ), hence the Raman features is similar to that of the CNT support. As the Ni/Cu ratio decreases (*i.e.*, higher Cu loadings), the  $I_{\text{D}}/I_{\text{G}}$  ratio increases suggesting that the produced carbon co-product has a higher defect density, which we speculate is caused by the larger diameter and wall thickness of the CNT co-product. The  $I_{\text{G}'}/I_{\text{G}}$  ratio decreases with the increase in Cu loading (*i.e.*, decrease in Ni/Cu ratio) which is consistent with the presence of multiwall CNT (multiwall CNT) with higher number of walls. The Raman observations are consistent with the (HAADF) STEM images which showed the formation of multiwall CNT with wider diameter (and wall thickness), Fig. 6 and 7. The larger diameter multiwall CNT were formed due to the restructuring of metal into larger domains and crystallite, which is also consistent with the XRD analysis.

The amount of Cu addition to Ni can therefore be directly correlated to both catalyst stability and quality of the carbon as evidenced by Raman spectroscopy. Fig. 9 compares both the  $I_{\text{D}}/I_{\text{G}}$  ratio of the carbon product and the deactivation rate

after reaction at 600 °C as a function of Cu mol fraction. A small increase in Cu mol fraction (*e.g.* 0.081; NiCu1/CNT) significantly reduced the deactivation rate constant from 2.77 to 0.42 h<sup>-0.5</sup> (85% decrease), while increasing the  $I_{\text{D}}/I_{\text{G}}$  ratio from 1.00 to 1.23 (23% increase). However, further increase in Cu loading had less effect on deactivation rate relative to the  $I_{\text{D}}/I_{\text{G}}$  ratio. For example, by nearly doubling the Cu mol fraction from 0.081 to 0.142 little change in deactivation rate was observed (0.48 *versus* 0.42). However, the  $I_{\text{D}}/I_{\text{G}}$  ratio increased from 1.23 to 1.41. The  $I_{\text{D}}/I_{\text{G}}$  ratio reached a plateau of  $\sim 1.9$  with Cu mol fractions between 0.35 and 0.55.

#### Effect of operation temperature on carbon co-product properties

As shown in Fig. 8b–d, both  $I_{\text{D}}/I_{\text{G}}$  and  $I_{\text{G}'}/I_{\text{G}}$  ratios change with reaction temperature as well as Ni/Cu ratio. Ni/CNT run at 550 °C showed slightly higher  $I_{\text{D}}/I_{\text{G}}$  ratio compared to that of the CNT support (1.23 and 1.11 respectively), suggesting



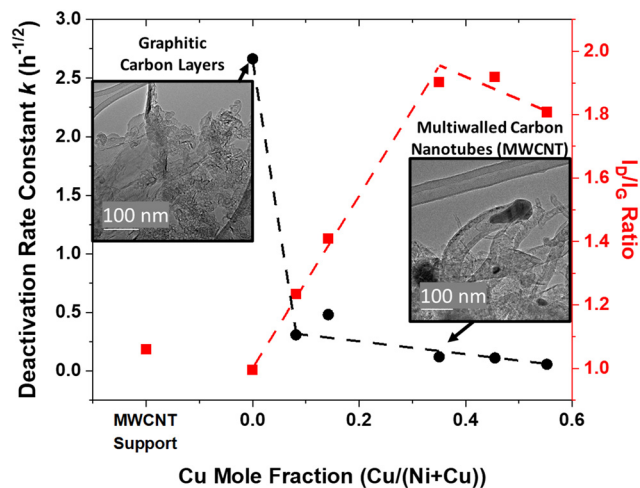


Fig. 9 Deactivation rate constant and Raman  $I_D/I_G$  ratio of resulting carbon product for NiCu<sub>x</sub>/CNT ( $x = 0, 0.6, 1, 2, 5, 10, 15$ ) catalysts prepared by solvothermal method at reaction temperature of 600 °C under 30 cm<sup>3</sup> min<sup>-1</sup> 30 vol% CH<sub>4</sub> in N<sub>2</sub>. The deactivation rate constants and  $I_D/I_G$  ratios are taken from Table 1 and Fig. 8, respectively.

that the properties of the CNT co-product generated are similar to that of the CNT support. The Raman spectra collected at higher reaction temperatures with 10Ni/CNT was similar to that of the CNT support because the catalyst had low carbon yield (at 600 °C) or was inactive (650 and 700 °C) due to the fast deactivation. NiCu1/CNT at 550 °C had similar TCD performance to 10Ni/CNT but showed a higher  $I_D/I_G$  ratio (1.79 and 1.23 respectively) highlighting the effect of Ni/Cu ratio on the carbon-coproduct morphology. At 600 °C, the NiCu1 TCD performance resembled that at 550 °C but the  $I_D/I_G$  ratio decreased from 1.79 to 1.23. We speculate this is partially caused by the change in metal particle size (Table S4†) via metal sintering resulting in the formation of CNT with different diameters and wall thicknesses. At 650 and 700 °C, the NiCu1/CNT  $I_D/I_G$  ratio further decreases to about 1.0 due to low carbon deposition, resulting in a near identical  $I_D/I_G$  ratio compared to the CNT support. NiCu15/CNT at 550 °C had similar TCD performance to NiCu1/CNT and had nearly identical  $I_D/I_G$  (1.78 and 1.79 respectively) and  $I_G/I_G$  (0.690 for both) regardless of the differences in the initial metal particle size and Ni/Cu composition. This result suggests that both catalytic systems might generate similar active sites (*i.e.*, larger metal particles) under reaction conditions resulting in similar CNT morphologies. At 600 and 650 °C, NiCu15/CNT remain active and stable for TCD and the resulting carbon co-product had similar  $I_D/I_G$  ratio (1.81 and 1.77 respectively) suggesting that the stabilized active was similar as at 550 °C. As shown in Table S5,† the crystallite sizes derived from XRD of the spent NiCu15/CNT catalysts remained similar regardless of the reaction temperature (between 17.2 and 21.4 nm), suggesting that the crystallite size is the main factor dictating the morphology of the carbon co-product. At 700 °C, NiCu15/CNT was the most active and stable catalyst tested but deactivated within 2 h of reaction, resulting in low

overall carbon deposition. Hence, the obtained Raman signal comes mostly from the CNT support as evidence by the similar  $I_D/I_G$  and  $I_G/I_G$  ratios of the NiCu15/CNT and support.

As shown in Table S5† the crystallite size (10.4 and 8.6 nm) and Ni/Cu molar ratio (0.676 and 0.790) of the spent NiCu15/CNT remained similar to that of the fresh catalyst suggesting that a fraction of the metal nanoparticles deactivated before restructuring into the larger crystallite needed to catalyze the stable TCD reaction. HAADF-STEM images of the NiCu15/CNT catalyst run at 700 °C confirms that the spent catalyst still had sections of intact  $\approx 10$  nm NiCu metal particle, Fig. S7.† This is also consistent with our previous work showing that  $>15$  nm particles are needed to catalyze the TCD reaction and selective CNT formation; however,  $\leq 10$  nm metal particles deactivate due to the preferential formation of graphitic layers (and metal particle blockage) as opposed to CNT.<sup>12</sup> Fig. 7 and S7b† confirmed that  $>50$  nm nanoparticles were still formed at 700 °C which explained the initial TCD. STEM images of the spent NiCu15/CNT at 700 °C reveal that the carbon co-product formed on the  $>50$  nm metal particles was primarily multiwall CNT with wall thickness  $>14$  nm. Hence, Cu serves dual purposes for the TCD reaction; 1) modifies the carbon co-product morphology to multiwall CNT and 2) causes the metal particles to restructure into larger metal particles, which are more stable for TCD at higher temperatures and selective towards the formation of multiwall CNT.

## Conclusions

We investigated the role of Cu in the TCD performance of NiCu/CNT catalysts. We determined that crystallite size, Ni/Cu ratio, and operating temperature were key factors for TCD activity, stability, and carbon coproduct morphology. NiCu catalyst synthesized with different Ni/Cu ratios offered different benefits as a function of reaction temperature. At 550 °C, there was a detrimental TCD activity effect with addition of Cu; however, the resulting carbon co-product had different properties. At 600 °C the addition of Cu benefitted the TCD activity and stability and modified the properties of the carbon co-product. At  $>650$  °C, only the catalyst with high Cu loading remained active and stable for TCD.

Characterization of the catalysts after reaction revealed that the addition of Cu to Ni results in the stabilization of larger metal nanoparticles, which are more stable for TCD at higher reaction temperatures and more selective towards CNT growth. In the absence of Cu, bamboo-shaped CNT was the main morphology observed and the addition of Cu resulted in a change in CNT morphology to multiwall CNT. In all cases, we observed the active site restructuring by the preferential segregation of Cu out of the NiCu alloy (*i.e.*, the Ni/Cu ratio increases) and change in metal particle size. At low Cu loadings (*i.e.*, high Ni/Cu ratio) the catalyst deactivated at reaction temperatures  $>600$  °C due to the encapsulation of the metal active sites before restructuring and loss of Cu. At high Cu loadings (*i.e.*, low Ni/Cu ratio),



reaction temperatures between 550 and 650 °C caused metal particle restructuring into <17 nm particles with higher Ni/Cu loading compared to the fresh catalyst, which resulted in the preferential multiwall CNT formation. Operation at 700 °C caused encapsulation of metal particles before being able to restructure, resulting in catalyst deactivation.

Hence, this work highlights how catalyst composition and operation conditions can be used to optimize catalyst stability and yield different carbon co-product morphologies generated during methane TCD.

## Author contributions

M. X. – conceptualization, methodology, data analysis, catalyst synthesis, catalyst characterization, catalyst test, original draft; J. A. L.-R. – conceptualization, methodology, data analysis, catalyst synthesis, catalyst testing, data analysis, draft editing; N. W. R – catalyst testing, catalyst characterization, data analysis; R. S. W. – data analysis, draft editing. M. E. B. – XRD analysis; L. K. – TEM and EDS characterization; C. J. – Raman characterization; J. H. – Discussion; R. A. D. – supervision, discussion, funding acquisition, draft editing.

## Conflicts of interest

The authors declare that they have no known competing financial interests or personal relationships that could have appeared to influence the work reported in this paper.

## Acknowledgements

This work was financially supported by the U.S. Department of Energy (DOE), Office of Energy Efficiency and Renewable Energy, Hydrogen and Fuel Cells Program, and performed at Pacific Northwest National Laboratory (PNNL) and in collaboration with the H2@Scale Consortium. Financial support also was provided by Southern California Gas Company and C4-MCP LLC through a Cooperative Research and Development Agreement. PNNL is a DOE national laboratory located in Richland, Washington. Some catalyst characterization studies were performed using the Environmental Molecular Sciences Laboratory, a DOE Office of Science User Facility sponsored by the Office of Biological and Environmental Research located at PNNL. The views and opinions of the authors expressed herein do not necessarily state or reflect those of the United States Government or any agency thereof. Neither the United States Government nor any agency thereof, nor any of their employees, makes any warranty, expressed or implied, or assumes any legal liability or responsibility for the accuracy, completeness, or usefulness of any information, apparatus, product, or process disclosed or represents that its use would not infringe privately owned rights.

## References

- 1 N. Muradov and T. Veziroğlu, From hydrocarbon to hydrogen-carbon to hydrogen economy, *Int. J. Hydrogen Energy*, 2005, **30**, 225–237.
- 2 J. Zhang, X. Li, H. Chen, M. Qi, G. Zhang, H. Hu and X. Ma, Hydrogen production by catalytic methane decomposition: Carbon materials as catalysts or catalyst supports, *Int. J. Hydrogen Energy*, 2017, **42**, 19755–19775.
- 3 U. Ashik, W. W. Daud and H. F. Abbas, Production of greenhouse gas free hydrogen by thermocatalytic decomposition of methane—A review, *Renewable Sustainable Energy Rev.*, 2015, **44**, 221–256.
- 4 R. M. Navarro, M. A. Peña and J. L. G. Fierro, Hydrogen Production Reactions from Carbon Feedstocks: Fossil Fuels and Biomass, *Chem. Rev.*, 2007, **107**, 3952–3991.
- 5 J. D. Holladay, J. Hu, D. L. King and Y. Wang, An overview of hydrogen production technologies, *Catal. Today*, 2009, **139**, 244–260.
- 6 N. Sánchez-Bastardo, R. Schlögl and H. Ruland, Methane Pyrolysis for Zero-Emission Hydrogen Production: A Potential Bridge Technology from Fossil Fuels to a Renewable and Sustainable Hydrogen Economy, *Ind. Eng. Chem. Res.*, 2021, **60**, 11855–11881.
- 7 N. Sánchez-Bastardo, R. Schlögl and H. Ruland, Methane Pyrolysis for CO<sub>2</sub>-Free H<sub>2</sub> Production: A Green Process to Overcome Renewable Energies Unsteadiness, *Chem. Ing. Tech.*, 2020, **92**, 1596–1609.
- 8 H. F. Abbas and W. M. A. Wan Daud, Hydrogen production by methane decomposition: A review, *Int. J. Hydrogen Energy*, 2010, **35**, 1160–1190.
- 9 Y. Li, D. Li and G. Wang, Methane decomposition to CO<sub>x</sub>-free hydrogen and nano-carbon material on group 8–10 base metal catalysts: A review, *Catal. Today*, 2011, **162**, 1–48.
- 10 J. X. Qian, T. W. Chen, L. R. Enakonda, D. B. Liu, G. Mignani, J.-M. Basset and L. Zhou, Methane decomposition to produce CO<sub>x</sub>-free hydrogen and nano-carbon over metal catalysts: A review, *Int. J. Hydrogen Energy*, 2020, **45**, 7981–8001.
- 11 X. Gao, Y. Wen, R. Tan, H. Huang and S. Kawi, A review of catalyst modifications for a highly active and stable hydrogen production from methane, *Int. J. Hydrogen Energy*, 2023, **48**, 6204–6232.
- 12 M. Xu, J. A. Lopez-Ruiz, L. Kovarik, M. E. Bowden, S. D. Davidson, R. S. Weber, I. W. Wang, J. Hu and R. A. Dagle, Structure sensitivity and its effect on methane turnover and carbon co-product selectivity in thermocatalytic decomposition of methane over supported Ni catalysts, *Appl. Catal., A*, 2021, **611**, 117967.
- 13 S. Karimi, F. Bibak, F. Meshkani, A. Rastegarpanah, J. Deng, Y. Liu and H. Dai, Promotional roles of second metals in catalyzing methane decomposition over the Ni-based catalysts for hydrogen production: A critical review, *Int. J. Hydrogen Energy*, 2021, **46**, 20435–20480.
- 14 A. Gamal, K. Eid, M. H. El-Naas, D. Kumar and A. Kumar, Catalytic Methane Decomposition to Carbon Nanostructures and CO<sub>x</sub>-Free Hydrogen: A Mini-Review, *Nanomaterials*, 2021, **11**, 1226.



- 15 M. Pudukudy, Z. Yaakob and Z. S. Akmal, Direct decomposition of methane over SBA-15 supported Ni, Co and Fe based bimetallic catalysts, *Appl. Surf. Sci.*, 2015, **330**, 418–430.
- 16 N. A. Hermes, M. A. Lansarin and O. W. Perez-Lopez, Catalytic decomposition of methane over M-Co-Al catalysts (M= Mg, Ni, Zn, Cu), *Catal. Lett.*, 2011, **141**, 1018–1025.
- 17 A. H. Fakeeha, W. U. Khan, A. S. Al-Fatesh, A. E. Abasaed and M. A. Naeem, Production of hydrogen and carbon nanofibers from methane over Ni-Co-Al catalysts, *Int. J. Hydrogen Energy*, 2015, **40**, 1774–1781.
- 18 G. Wang, Y. Jin, G. Liu and Y. Li, Production of hydrogen and nanocarbon from catalytic decomposition of methane over a Ni-Fe/Al<sub>2</sub>O<sub>3</sub> catalyst, *Energy Fuels*, 2013, **27**, 4448–4456.
- 19 S. Takenaka, Y. Shigeta, E. Tanabe and K. Otsuka, Methane decomposition into hydrogen and carbon nanofibers over supported Pd-Ni catalysts, *J. Catal.*, 2003, **220**, 468–477.
- 20 G. D. B. Nuernberg, H. V. Fajardo, E. L. Foletto, S. M. Hickel-Probst, N. L. Carreño, L. F. Probst and J. Barrault, Methane conversion to hydrogen and nanotubes on Pt/Ni catalysts supported over spinel MgAl<sub>2</sub>O<sub>4</sub>, *Catal. Today*, 2011, **176**, 465–469.
- 21 A. E. Awadallah, A. A. Aboul-Enein and A. K. Aboul-Gheit, Various nickel doping in commercial Ni-Mo/Al<sub>2</sub>O<sub>3</sub> as catalysts for natural gas decomposition to CO<sub>x</sub>-free hydrogen production, *Renewable Energy*, 2013, **57**, 671–678.
- 22 N. Bayat, M. Rezaei and F. Meshkani, Hydrogen and carbon nanofibers synthesis by methane decomposition over Ni-Pd/Al<sub>2</sub>O<sub>3</sub> catalyst, *Int. J. Hydrogen Energy*, 2016, **41**, 5494–5503.
- 23 N. Gutta, V. K. Velisoju, A. Chatla, V. Boosa, J. Tardio, J. Patel and V. Akula, Promotional Effect of Cu and Influence of Surface Ni-Cu Alloy for Enhanced H<sub>2</sub> Yields from CH<sub>4</sub> Decomposition over Cu-Modified Ni Supported on MCM-41 Catalyst, *Energy Fuels*, 2018, **32**, 4008–4015.
- 24 D. Torres, J. L. Pinilla and I. Suelves, Screening of Ni-Cu bimetallic catalysts for hydrogen and carbon nanofilaments production via catalytic decomposition of methane, *Appl. Catal., A*, 2018, **559**, 10–19.
- 25 J. Chen, Y. Li, Y. Ma, Y. Qin and L. Chang, Formation of bamboo-shaped carbon filaments and dependence of their morphology on catalyst composition and reaction conditions, *Carbon*, 2001, **39**, 1467–1475.
- 26 V. Jourdain and C. Bichara, Current understanding of the growth of carbon nanotubes in catalytic chemical vapour deposition, *Carbon*, 2013, **58**, 2–39.
- 27 Y. Echehoven, I. Suelves, M. Lázaro, M. Sanjuán and R. Moliner, Thermo catalytic decomposition of methane over Ni-Mg and Ni-Cu-Mg catalysts: effect of catalyst preparation method, *Appl. Catal., A*, 2007, **333**, 229–237.
- 28 M. J. Lázaro, Y. Echehoven, I. Suelves, J. M. Palacios and R. Moliner, Decomposition of methane over Ni-SiO<sub>2</sub> and Ni-Cu-SiO<sub>2</sub> catalysts: Effect of catalyst preparation method, *Appl. Catal., A*, 2007, **329**, 22–29.
- 29 H. Y. Wang and A. C. Lua, Methane decomposition using Ni-Cu alloy nano-particle catalysts and catalyst deactivation studies, *Chem. Eng. J.*, 2015, **262**, 1077–1089.
- 30 Y. Shen, M. Ge and A. C. Lua, Deactivation of bimetallic nickel-copper alloy catalysts in thermocatalytic decomposition of methane, *Catal. Sci. Technol.*, 2018, **8**, 3853–3862.
- 31 Y. Shen and A. C. Lua, Synthesis of Ni and Ni-Cu supported on carbon nanotubes for hydrogen and carbon production by catalytic decomposition of methane, *Appl. Catal., B*, 2015, **164**, 61–69.
- 32 L. Avdeeva, O. Goncharova, D. Kochubey, V. Zaikovskii, L. Plyasova, B. Novgorodov and S. K. Shaikhutdinov, Coprecipitated Ni-alumina and Ni-Cu-alumina catalysts of methane decomposition and carbon deposition. II. Evolution of the catalysts in reaction, *Appl. Catal., A*, 1996, **141**, 117–129.
- 33 T. V. Reshetyenko, L. B. Avdeeva, Z. R. Ismagilov, A. L. Chuvilin and V. A. Ushakov, Carbon capacious Ni-Cu-Al<sub>2</sub>O<sub>3</sub> catalysts for high-temperature methane decomposition, *Appl. Catal., A*, 2003, **247**, 51–63.
- 34 I. González, J. C. De Jesus, C. U. de Navarro and M. García, Effect of Cu on Ni nanoparticles used for the generation of carbon nanotubes by catalytic cracking of methane, *Catal. Today*, 2010, **149**, 352–357.
- 35 I. W. Wang, R. A. Dagle, T. S. Khan, J. A. Lopez-Ruiz, L. Kovarik, Y. Jiang, M. Xu, Y. Wang, C. Jiang, S. D. Davidson, P. Tavadze, L. Li and J. Hu, Catalytic decomposition of methane into hydrogen and high-value carbons: combined experimental and DFT computational study, *Catal. Sci. Technol.*, 2021, **11**, 4911–4921.
- 36 J. Chen, Y. Li, Z. Li and X. Zhang, Production of CO<sub>x</sub>-free hydrogen and nanocarbon by direct decomposition of undiluted methane on Ni-Cu-alumina catalysts, *Appl. Catal., A*, 2004, **269**, 179–186.
- 37 S. K. Saraswat and K. K. Pant, Ni-Cu-Zn/MCM-22 catalysts for simultaneous production of hydrogen and multiwall carbon nanotubes via thermo-catalytic decomposition of methane, *Int. J. Hydrogen Energy*, 2011, **36**, 13352–13360.
- 38 Y. Li, J. Chen, L. Chang and Y. Qin, The Doping Effect of Copper on the Catalytic Growth of Carbon Fibers from Methane over a Ni/Al<sub>2</sub>O<sub>3</sub> Catalyst Prepared from Feitknecht Compound Precursor, *J. Catal.*, 1998, **178**, 76–83.
- 39 J. Li, C. Xiao, L. Xiong, X. Chen, L. Zhao, L. Dong, Y. Du, Y. Yang, H. Wang and S. Peng, Hydrogen production by methane decomposition over Ni-Cu-SiO<sub>2</sub> catalysts: effect of temperature on catalyst deactivation, *RSC Adv.*, 2016, **6**, 52154–52163.
- 40 Y. Li, J. Chen, Y. Ma, J. Zhao, Y. Qin and L. Chang, Formation of bamboo-like nanocarbon and evidence for the quasi-liquid state of nanosized metal particles at moderate temperatures, *Chem. Commun.*, 1999, 1141–1142.
- 41 H. Wang and R. T. K. Baker, Decomposition of methane over a Ni-Cu-MgO catalyst to produce hydrogen and carbon nanofibers, *J. Phys. Chem. B*, 2004, **108**, 20273–20277.
- 42 A. Hornés, P. Bera, M. Fernández-García, A. Guerrero-Ruiz and A. Martínez-Arias, Catalytic and redox properties of bimetallic Cu-Ni systems combined with CeO<sub>2</sub> or Gd-doped CeO<sub>2</sub> for methane oxidation and decomposition, *Appl. Catal., B*, 2012, **111**, 96–105.



- 43 Y. Echegoyen, I. Suelves, M. Lazaro, R. Moliner and J. Palacios, Hydrogen production by thermocatalytic decomposition of methane over Ni-Al and Ni-Cu-Al catalysts: Effect of calcination temperature, *J. Power Sources*, 2007, **169**, 150–157.
- 44 G. Naresh, V. V. Kumar, C. Anjaneyulu, J. Tardio, S. Bhargava, J. Patel and A. Venugopal, Nano size H $\beta$  zeolite as an effective support for Ni and NiCu for CO<sub>x</sub> free hydrogen production by catalytic decomposition of methane, *Int. J. Hydrogen Energy*, 2016, **41**, 19855–19862.
- 45 N. Bayat, M. Rezaei and F. Meshkani, Methane decomposition over Ni-Fe/Al<sub>2</sub>O<sub>3</sub> catalysts for production of CO<sub>x</sub>-free hydrogen and carbon nanofiber, *Int. J. Hydrogen Energy*, 2016, **41**, 1574–1584.
- 46 I. Suelves, M. Lázaro, R. Moliner, Y. Echegoyen and J. Palacios, Characterization of NiAl and NiCuAl catalysts prepared by different methods for hydrogen production by thermo catalytic decomposition of methane, *Catal. Today*, 2006, **116**, 271–280.
- 47 A. C. Lua and H. Y. Wang, Decomposition of methane over unsupported porous nickel and alloy catalyst, *Appl. Catal., B*, 2013, **132–133**, 469–478.
- 48 J. Riley, C. Atallah, R. Siriwardane and R. Stevens, Technoeconomic analysis for hydrogen and carbon Co-Production via catalytic pyrolysis of methane, *Int. J. Hydrogen Energy*, 2021, **46**, 20338–20358.
- 49 R. Dagle, V. Dagle, M. Bearden, J. Holladay, T. Krause and S. Ahmed, R&D opportunities for development of natural gas conversion technologies for co-production of hydrogen and value-added solid carbon products, Argonne National Lab Report, 2017.
- 50 A. F. A. S. Muhammad, A. Awad, R. Saidur, N. Masiran, A. Salam and B. Abdullah, Recent advances in cleaner hydrogen productions via thermo-catalytic decomposition of methane: Admixture with hydrocarbon, *Int. J. Hydrogen Energy*, 2018, **43**, 18713–18734.
- 51 W. Chen, Z. Fan, X. Pan and X. Bao, Effect of confinement in carbon nanotubes on the activity of Fischer–Tropsch iron catalyst, *J. Am. Chem. Soc.*, 2008, **130**, 9414–9419.
- 52 W. Chen, X. Pan and X. Bao, Tuning of redox properties of iron and iron oxides via encapsulation within carbon nanotubes, *J. Am. Chem. Soc.*, 2007, **129**, 7421–7426.
- 53 M. Xu, J. A. Lopez-Ruiz, L. Kovarik, M. E. Bowden, S. D. Davidson, R. S. Weber, I.-W. Wang, J. Hu and R. A. Dagle, Structure sensitivity and its effect on methane turnover and carbon co-product selectivity in thermocatalytic decomposition of methane over supported Ni catalysts, *Appl. Catal., A*, 2021, **611**, 117967.
- 54 A. Voorhies Jr., Carbon Formation in Catalytic Cracking, *Ind. Eng. Chem.*, 1945, **37**, 318–322.
- 55 G. F. Froment and K. B. Bischoff, Non-steady state behaviour of fixed bed catalytic reactors due to catalyst fouling, *Chem. Eng. Sci.*, 1961, **16**, 189–201.
- 56 M. A. Turchanin, P. G. Agraval and A. R. Abdulov, Phase equilibria and thermodynamics of binary copper systems with 3d-metals. VI. Copper-nickel system, *Powder Metall. Met. Ceram.*, 2007, **46**, 467–477.
- 57 M. Xu, J. A. Lopez-Ruiz, L. Kovarik, M. E. Bowden, S. D. Davidson, R. S. Weber, I. W. Wang, J. Hu and R. A. Dagle, Structure sensitivity and its effect on methane turnover and carbon co-product selectivity in thermocatalytic decomposition of methane over supported Ni catalysts, *Appl. Catal., A*, 2021, **611**, 117967.
- 58 D. A. Kutteri, I.-W. Wang, A. Samanta, L. Li and J. Hu, Methane decomposition to tip and base grown carbon nanotubes and CO<sub>x</sub>-free H<sub>2</sub> over mono-and bimetallic 3d transition metal catalysts, *Catal. Sci. Technol.*, 2018, **8**, 858–869.
- 59 J.-B. Wu, M.-L. Lin, X. Cong, H.-N. Liu and P.-H. Tan, Raman spectroscopy of graphene-based materials and its applications in related devices, *Chem. Soc. Rev.*, 2018, **47**, 1822–1873.
- 60 J. Hodkiewicz and T. Scientific, Characterizing carbon materials with Raman spectroscopy, Thermo Scientific Application Note, 51946, 2010.
- 61 C. Palmer, E. Bunyan, J. Gelinas, M. J. Gordon, H. Metiu and E. W. McFarland, CO<sub>2</sub>-Free Hydrogen Production by Catalytic Pyrolysis of Hydrocarbon Feedstocks in Molten Ni-Bi, *Energy Fuels*, 2020, **34**, 16073–16080.

